

1 Millikelvin-precision temperature sensing for advanced
2 cryogenic detectors

3 M. Antonova^a, J. Capó^a, A. Cervera^a, P. Fernández^{a,2}, M. Á. García-Peris^{a,1,*}, X.
4 Pons^b

^a*Instituto de Fisica Corpuscular Catedratico Jose Beltran 2 E-46980 Paterna (Valencia) Spain*

^b*CERN Espl. des Particules 1 1211 Meyrin Switzerland*

5 **Abstract**

6 Precise temperature monitoring —to the level of a few milli-Kelvin— is essential for
7 the operation of large-scale cryostats requiring a recirculation system. In particular, the
8 performance of Liquid Argon Time Projection Chambers —such as those planned for the
9 DUNE experiment— strongly relies on proper argon purification and mixing, which can
10 be characterized by a sufficiently dense grid of high-precision temperature probes. In this
11 article, we present a novel technique for the cross-calibration of Resistance Temperature
12 Detectors in cryogenic liquids, developed as part of the temperature monitoring system
13 for a DUNE prototype. This calibration has enabled the validation and optimization of
14 the system’s components, achieving an unprecedented precision of 2.5 mK.

15 **Keywords:** Detectors, Liquid Argon, Cryogenics, Temperature, RTD, Purity,
16 Computational Fluid Dynamics

17 **1. Introduction**

18 Precise temperature sensing is essential in large cryogenic detectors, where the circulation
19 and purification of cryogenic liquids significantly impact overall detector performance.
20 Uncontrolled temperature gradients in such systems can disrupt the cryostat dynamics
21 and ultimately affect the experiment’s physics sensitivity. In this work, we present the

*Corresponding author

Email address: miguel.garcia-peris@manchester.ac.uk (M. Á. García-Peris)

¹now in the University of Manchester

²now at Donostia International Physics Center, DIPC

22 calibration procedure of a novel temperature monitoring system developed for a prototype
23 of the future DUNE experiment. This procedure has been essential for ensuring accurate
24 measurements and for validating and optimizing the various components of the system.

25 DUNE, which stands for Deep Underground Neutrino Experiment [1], is expected
26 to begin taking data toward the end of the decade. It aims to perform comprehen-
27 sive neutrino oscillation analyses —broadly exploring the Charge-Parity (CP) violation
28 parameters phase-space and resolving the neutrino-mass hierarchy problem [2]. Its ex-
29 tense physics program also includes searches for hypothetical proton decay channels [3],
30 multi-messenger astronomy from supernovae and neutrino bursts [4], and explorations
31 of Beyond the Standard Model (BSM) physics [5]. Utilizing the most powerful neutrino
32 beam ever constructed, generated at Fermilab, the experiment adopts a long-baseline
33 neutrino oscillation approach with two detectors. The Near Detector, also at Fermilab,
34 will characterize the unoscillated neutrino beam. The Far Detector (FD), located in the
35 Sandford Underground Research Facility (SURF), 1300 km away from the ND and 1.5
36 km underground, will measure the oscillated flux.

37 In the Phase I, DUNE Far Detector will consist of two Liquid Argon Time Projection
38 Chambers (LArTPCs) and is anticipated to begin operations by 2029. DUNE phase II
39 will complement with two more modules by mid 30's, aiming at a total fiducial mass of
40 40 kilotonnes. The detector technology has been established, with excellent tracking and
41 calorimetric capabilities, in several smaller-scale experiments [6, 7]. The first demonstra-
42 tion of the technology at the kilotonne scale has been carried out at the CERN Neutrino
43 Platform as part of the ProtoDUNE program. In particular, the ProtoDUNE Single-
44 Phase (SP) experiment [8] replicated the components of the DUNE FD Horizontal Drift
45 (HD) [9] configuration at a scale 1:1, using a total argon mass 20 times smaller (770
46 tonnes). It was operated from mid-2018 to mid-2020, constituting the largest monolithic
47 LArTPC to ever constructed and operated up to date [10, 11].

48 During ProtoDUNE-SP operation, the level of impurities was kept way below 100 ppt
49 oxygen equivalent using a cryogenic recirculation and purification system [8, 11]. This is
50 critical in an LArTPC, as the 3D images generated by charged particles traversing the
51 detector can be significantly degraded by impurities in the medium—such as nitrogen,
52 oxygen, and water—which absorb ionization electrons, thereby deteriorating spatial res-

53 olution and introducing biases in energy measurements. Three purity monitors, based
54 on the ICARUS design [12], were installed outside the active volume of the TPC to
55 measure the electron lifetime, which is inversely related to the residual concentration of
56 impurities. They ran twice a day to monitor the argon purity and thus to provide the
57 necessary corrections for posterior data analysis.

58 Achieving the necessary argon purity has been possible thanks to the studies based
59 on computational fluid dynamic (CFD) simulations, and the experience gained with
60 previous LArTPC demonstrators such as LAPD [13] and the 35-tonne prototype [14, 15],
61 which have paved the way to operate large-scale cryostats requiring low concentrations
62 of impurities. These studies have also shown that it exists a strong correlation between
63 temperature and purity in the liquid argon volume. The distribution of impurities is
64 insensitive to small ($\mathcal{O} \sim 1$ K) absolute temperature variations, but strongly depends on
65 the relative vertical temperature gradient. Since the bulk volume in the cryostats must
66 be continuously mixed with the incoming purified argon to ensure uniform purification
67 of the entire LAr volume, the temperature distribution serves as a clear indicator of
68 the mixing process: a homogeneous temperature distribution suggests proper mixing,
69 while large temperature gradients signal inadequate mixing. If the LAr bulk volume is
70 not mixed appropriately, a stratification regime can develop: a significant portion of the
71 liquid remains unpurified, generating ‘dead’ regions inside the detector. Thus, continuous
72 monitoring of this temperature gradient can identify and mitigate potential failures of
73 the purification system. In ProtoDUNE-SP, this gradient was predicted to be about 15
74 mK by the CFD simulations [8, 9].

75 Even with homogeneous mixing, the CFD simulations predict that the concentration
76 of impurities may vary across the cryostat volume, requiring a position-dependent correc-
77 tion to the electron lifetime. The Purity Monitors themselves are intrusive objects which
78 cannot be deployed inside the active volume, but rather only at a few well-defined loca-
79 tions near the cryostat walls; thus, precise inference of the electron lifetime map requires
80 alternative methods, as the one proposed in this article. A net of temperature sensors
81 cross-calibrated to the <5 mK level should allow the measurement of a 15 mK tempera-
82 ture gradient, which can be used to constrain CFD simulations, providing a data-driven
83 prediction of the impurity concentration. The main limitations of this new approach are

84 the precision of the cross-calibration of the temperature sensors and the accuracy of the
85 simulations. In this article, precise temperature monitoring for ProtoDUNE-SP will be
86 described, with particular emphasis on sensor calibration in the laboratory.

87 **2. The temperature monitoring system of ProtoDUNE-SP**

88 ProtoDUNE-SP [8] was the Single-Phase demonstrator of DUNE Far Detector HD mod-
89 ule [9]. The elements constituting the TPC, its associated readout electronics and the
90 photon detection system, were housed in a $8 \times 8 \times 8 \text{ m}^3$ cryostat that contained the LAr that
91 served both as target and detector material. The cryostat, a free-standing steel-framed
92 vessel with an insulated double membrane, is based on the technology used for liquefied
93 natural gas storage and transport. A cryogenic system maintains the LAr at a stable
94 temperature of about 87 K by operating at a slight and constant over-pressure. It also
95 ensures the required purity level by means of a closed-loop process that recovers the evap-
96 orated argon, recondenses it, filters it, and recirculates it back into the cryostat, keeping
97 the LAr level at about 7.3 m from the bottom membrane. ProtoDUNE-SP was exposed
98 to a charged particle test-beam from October to November 2018, and later recorded cos-
99 mic rays until January 2020 [10, 11]. It was finally emptied and decommissioned during
100 Summer 2020.

101 In order to understand the LAr behaviour inside the cryostat and validate the CFD
102 simulations, 92 high-precision temperature sensors were installed inside ProtoDUNE-SP,
103 near the active volume. These sensors were distributed in two vertical arrays, or Tem-
104 perature Gradient Monitors (TGM), and two horizontal grids below and above the TPC,
105 respectively. Three elements were common to all systems: sensors, cables and readout
106 electronics. Resistance Temperature Detector (RTD) technology [16] was chosen for this
107 application. It consists of a metallic element whose resistance changes with temperature.
108 This resistance is measured by feeding the RTD with a known current and measuring the
109 resulting voltage. Based on previous experience from other prototypes [14], Lake Shore
110 PT102 platinum sensors [17] with 100Ω resistance at room temperature were chosen.
111 Sensors were mounted on a $52 \times 14 \text{ mm}^2$ PCB with an IDC-4 connector manufactured by
112 Molex [18, 19], such that they could be plugged-in at any time. Several versions of the
113 PCB have been explored, finally converging to the one shown in Fig. 1, which minimizes

114 the contact of the sensor with the PCB while keeping the sensor protected.

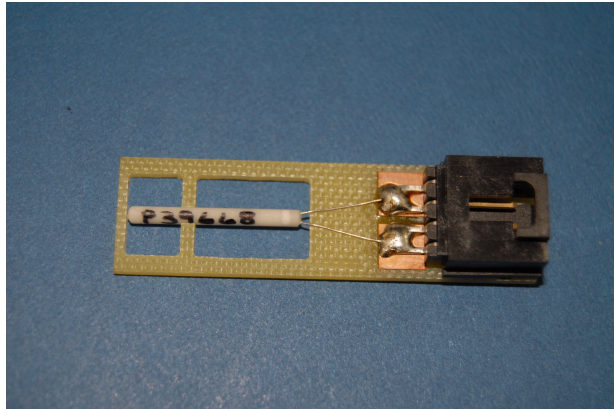


Figure 1: PCB support with temperature sensor and IDC-4 connector. The transition from two wires at the sensor to 4 wires at the readout is clearly seen. The sensor has a length of 2 cm.

115 A careful choice of the readout cable and the connections are essential to obtain the
116 required temperature precision. See for example Ref. [16] for a detailed description. A
117 custom cable made by Axon [20] was used. It consists of four American Wire Gauge
118 (AWG) 28 teflon-jacketed copper wires, forming two twisted pairs, with a metallic ex-
119 ternal shield and an outer teflon jacket. The outer diameter of the cable is 3.7 mm.
120 Teflon was chosen for its good thermal properties and low out-gassing. The metallic
121 external shield (connected to the readout in one end and left floating at the sensor's end)
122 and the twisted pairs are crucial to reduce the effect of external electromagnetic noise
123 pick-up. When RTDs are far from the voltmeter, the resistance of cables and connectors
124 are added to the one of the sensor, biasing the temperature measurement. This bias
125 can be subtracted to some level, but cannot be fully controlled since the resistance of
126 those elements also depends on temperature. To minimise the impact of this effect a four
127 wire-terminal readout is employed [16], such that the voltage is measured in the vicinity
128 of the RTD.

129 The last common element is the readout system, consisting of a very precise 1 mA
130 current source to excite the sensors and a 24 bits ADC to measure the voltage. The
131 readout system will be described in detail in Section 3.

132 As previously mentioned, ProtoDUNE-SP CFD simulations predict vertical tempera-

ture gradients as low as 15 mK [8]. A relative precision better than 5 mK was required to validate and tune those simulations with sufficient confidence. Three main ingredients are necessary to obtain such a precision: i) cryogenically rated, high-accuracy temperature probes suitable for LAr applications., ii) a very precise readout system, and iii) accurate and stable long-term calibration, both for the readout and the sensors. As mentioned above, two TGMs were deployed in ProtoDUNE-SP: one could be moved vertically and hence calibrated *in situ*, while the other one —static— fully relied on a prior calibration in the laboratory. In this article, the calibration of the static TGM [21] sensors is described in detail. This device consists of a vertical array of 48 sensors, installed 20 cm away from the lateral field cage.

The calibration was performed once in spring 2018 (a few months before the operation of ProtoDUNE-SP), and several times after ProtoDUNE-SP decommissioning. In this article the calibration setup, procedure and results will be described in detail. Comparison between the different calibration campaigns will be addressed, revealing important information about systematic uncertainties and RTD ageing.

3. Readout system

A precise and stable electronic readout system is needed to achieve the required precision. In previous versions of the calibration system, each sensor was connected to a different and independent electronic circuit and thus, fed by a different current and read by a different ADC channel. It was soon realized that the measured temperature difference between any two pairs of sensors was heavily affected by the electronic offset between channels. This offset was not constant, and showed dependence on ambient temperature and humidity, which affected both the current source and the ADC, generating variations of tens of mK for the measurement of a single calibration constant between two sensors. A modified version of an existing PT100 mass temperature readout system, developed at CERN for one of the LHC experiments [22], was adapted to address this issue. The system consists of an electronic circuit that includes:

- A precise and accurate 1 mA current source for the excitation of the temperature sensors based on an application of the Texas Instruments precise voltage reference

162 REF102CU with a possibility to adjust $\pm 10\text{nA}$ with Keithley 2001 multimeter [23,
163 24].

- 164 • A multiplexing circuit based on the Analog Devices ADG1407BRUZ multiplexer
165 with ultralow internal resistance in an 8-channel differential configuration. By in-
166 tegrating three multiplexers, the readout circuit supports simultaneous acquisition
167 from 24 channels. The multiplexing circuit and the current source are assembled
168 on a single card (see Fig. 2).
- 169 • A readout system based on National Instruments Compact RIO-FPGA device [25]
170 equipped with a NI-9238 analogue input module that provide 24 bits resolution over
171 1 volt range [26]. By programming the Van Dusen equation the readout calculates
172 the temperature in Kelvin units. The Compact RIO also drives the control bits of
173 the multiplexers

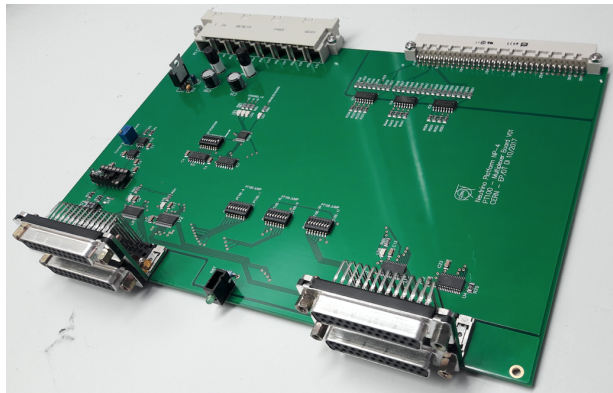


Figure 2: Current source and multiplexing card with 24 channels.

174 One of the features of the readout circuit is the serialization of the current source ex-
175 citation for all the sensors connected to the same board, such that the same current is
176 delivered to all of them. Multiplexing the signal of the sensors such that they can be
177 readout by the same ADC channel minimises the residual offset due to the electronics.
178 This system was used during the calibration campaigns presented in this article and also
179 for the temperature measurements during ProtoDUNE-SP operation.

180 The readout was not considered a potential source of bias during the calibration
181 campaign prior to the installation in ProtoDUNE-SP (see Sec. 4) and it was not studied

182 in detail at that time. However, in order to improve the calibration results following
 183 ProtoDUNE-SP operation, a more detailed study of the readout system was conducted
 184 prior to the calibration campaigns presented in 5. In particular, the twelve channels
 185 (7-18) used for sensor calibration were investigated. It was found that, despite the use of
 186 the multiplexing system, a small residual offset between channels persists. Fig. 3 shows
 187 the offsets of channels 8-18 with respect to channel 7, computed using twelve 20-ohm
 188 precision resistors with a low Temperature Coefficient of Resistance (TCR)³ precision
 189 resistors, with an equivalent temperature of 76 K. Two of those, High Precision 1 (HP1)
 190 and High Precision 2 (HP2), are selected as the measurement samples and connected
 191 to the reference channel (7) and the channel being calibrated (from 8-18), while leaving
 192 all other channels connected to other secondary resistors to let the current flow through
 193 the system. The readout offset between channel 7 and channel X, $\Delta T_{7-X}^{readout}$, is then
 194 computed using the results of two consecutive measurements:

- 195 1. HP1 in channel 7 and HP2 in the channel X being calibrated. The offset between
 196 the measured temperatures is

$$\Delta T_{7-X}^A = T_X^{HP2} - T_7^{HP1} + \Delta T_{7-X}^{readout}. \quad (1)$$

- 197 2. HP2 channel 7 and HP1 in the channel X being calibrated. The offset between the
 198 measured temperatures is

$$\Delta T_{X-7}^B = T_X^{HP1} - T_7^{HP2} + \Delta T_{7-X}^{readout}. \quad (2)$$

199 Because of the very low TCR of the resistors, it can be assumed that the resistances
 200 are constants in these two measurements ($T_7^{HP1} = T_X^{HP1}$ and $T_7^{HP2} = T_X^{HP2}$). Thus,
 201 the offset between channels 7 and X can be computed as the average between those two
 202 measurements:

$$\Delta T_{7-X}^{readout} = \frac{\Delta T_{7-X}^A + \Delta T_{X-7}^B}{2}. \quad (3)$$

³The temperature coefficient of resistance is defined as the change in resistance per unit resistance per degree rise in temperature. Typically $\pm 5\text{ppm}/^\circ\text{C}$.

203 The results in Fig. 3, show an offset of up to 2.5 mK when comparing directly with
 204 channel 7, while the offset between any other two channels is below 1 mK, indicating
 205 a special feature of this channel. Error bars in that figure correspond to the standard
 206 deviation of four independent measurements (repeatability) of the same offset (see Fig. 3).
 207 As it can be observed the error is below 0.5 mK, what probes the great repeatability of
 208 the readout. These offsets are more likely due to parasitic resistances in the different
 209 lines that are multiplexed. This finding allowed a correction to the measurements taken
 210 during the subsequent calibration campaigns, improving the obtained precision.

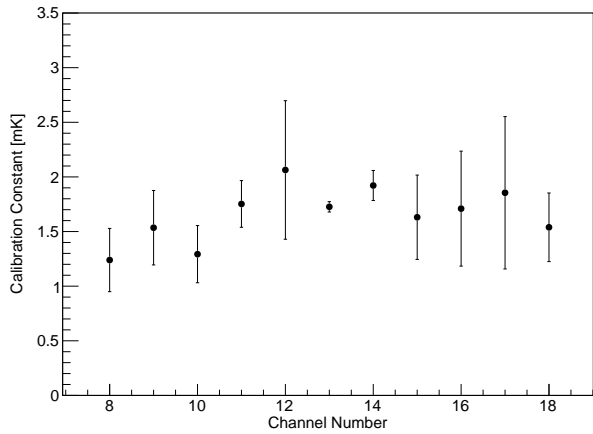


Figure 3: Offset between readout channels 8-18 and channel 7, used as reference. Points correspond to the mean of the 4 independent measurements and the error bars are their standard deviation.

211 4. Calibration before the installation in ProtoDUNE-SP

212 The Lake Shore Cryotronics company provides PT102 RTDs with a temperature ac-
 213 curacy of about 0.1 K, which is insufficient for ProtoDUNE-SP's requirements. While
 214 the company offers additional calibration to the 10 mK level, the cost is prohibitive.
 215 R&D on sensor calibration was identified as a crucial ingredient for the success of the
 216 ProtoDUNE-SP temperature monitoring system. For this particular application, sensor
 217 calibration consists in finding the temperature offset between any pair of sensors when
 218 exposing them to the same temperature. The experimental setup used for the calibra-
 219 tion of RTDs before their installation in ProtoDUNE-SP had two main components: i)

the readout system used to monitor the sensor's temperature (described in the previous section) and ii) the cryogenics vessel and the associated mechanical elements used to put sensors together under stable and homogeneous cryogenics conditions. They were developed to achieve a relative calibration with a precision better than 5 mK.

4.1. Experimental setup

The mechanics of the calibration setup evolved significantly from the initial tests to the final Static TGM calibration campaign. This evolution was primarily driven by the need to improve offset stability and repeatability. The final configuration (see Fig. 4) consisted of the following components:

- A polystyrene vessel formed by an outer box with dimensions $35 \times 35 \times 30 \text{ cm}^3$ and 4.5 cm thick walls, and a dedicated polystyrene cover, complemented by extruded polystyrene panels glued into the inner walls and floor of the outer box, to conform an inner empty volume of $10 \times 10 \times 20 \text{ cm}^3$.
- A $10 \times 10 \times 20 \text{ cm}^3$ 3D printed polylactic acid (PLA) box with two independent concentric volumes, placed in the inner volume of the polystyrene vessel. Its purpose is twofold: i) to contain LAr, since polystyrene is porous to it, and ii) to create an smaller inner volume with further insulation and less convection.
- A cylindrical aluminum capsule, to be placed in the inner volume of the PLA box, with 5 cm diameter, 12 cm height and 1 mm thin walls. It had a circular aluminum cover with a small opening to extract the cables and to allow LAr to penetrate inside. The capsule was used to slowly bring sensors to cryogenic temperatures by partial immersion in LAr with no liquid inside, minimizing thermal stress. Aluminum was chosen for its high thermal conductivity.
- A 3D printed PLA support for four sensors, to be placed inside the aluminum capsule, keeping sensors always in the same position with respect to each other and to the capsule walls.

The system described above ensures sufficiently stable and homogeneous conditions within the inner volume, with three levels of insulation: the outer polystyrene vessel and two PLA box LAr volumes. The aluminium capsule is key to this system and its usage

249 constituted a turning point in the R&D since it minimises thermal shocks, which were
 250 identified as the main limiting factor for the repeatability of the sensor's offsets. Indeed,
 251 variations of several tenths of mK were observed during initial tests without the capsule.
 252 The problem was attributed to thermal shocks when, after many immersions in LN₂, one
 253 of the sensors suffered a dramatic change in its offset (see Fig. 5). Examination at the
 254 microscope revealed cracks in the outer RTD ceramics (see Fig. 6).



Figure 4: Final calibration setup. Left: polystyrene box with PLA box and aluminum capsule. Middle: aluminum capsule. Right: Sensor's support with four sensors.

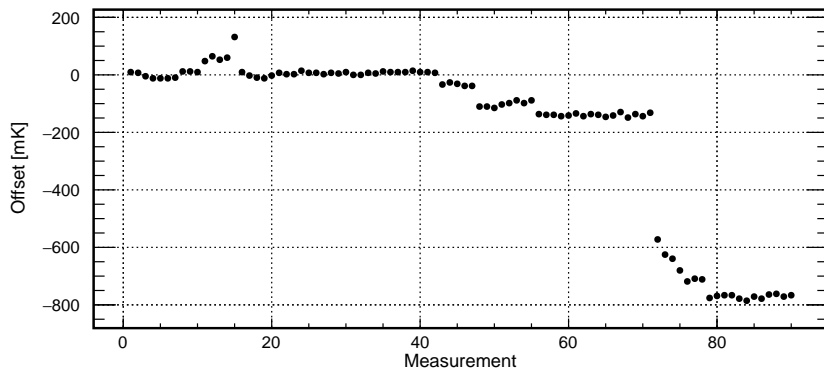


Figure 5: Offset between two sensors for 90 immersions in LN₂. A temperature drop of approximately 800 mK is observed around the 70th immersion point.

255 4.2. Calibration procedure

256 The calibration procedure relies on the assumption that all sensors in the capsule are at
 257 the same temperature. This limits the number of RTDs in a single run to four, since
 258 i) they should be as close as possible to each other and ii) as far as possible from the
 259 capsule walls (the sensor closer to the wall could be biased). Two different methods,

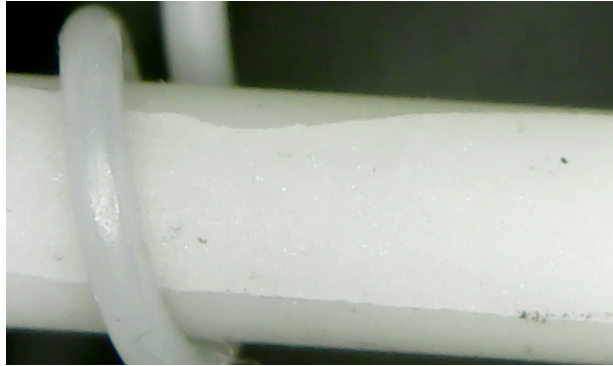


Figure 6: Cracks observed with the microscope in the ceramic of the sensor.

described schematically in Fig. 7, were used to cross-calibrate all 48 sensors in runs of 4 sensors:

1. **Reference method:** all sensors are calibrated with respect to a reference one, in sets of three sensors (the fourth one would be the reference sensor, which must be present in all runs). In total there are sixteen calibration sets.
2. **Tree method:** Four different sets of sensors can be cross-calibrated by performing a second round of measurements with a single promoted sensor from each of those four sets. Since there are 16 sets in total, a third round of measurement is needed to cross-calibrate the four sets in the second round.

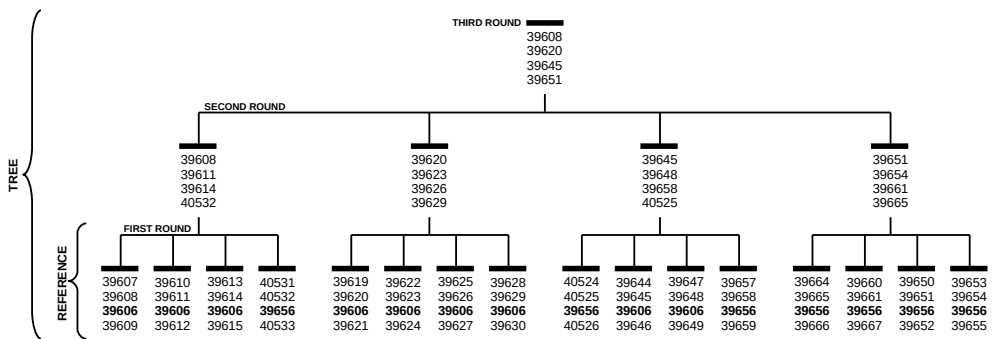


Figure 7: Schematic view of calibration sequence. Each number represents a different RTD, and the numbers in bold represent the reference sensors. The first round consists on a direct calibration respect to a reference sensor. The second and third rounds are needed to relate all sensors independently of the reference sensor.

The reference method was expected to be more precise since any two sensors were

270 related through a single intermediate sensor (the reference one), while for the tree method
 271 the relation between any two sensors required more than one intermediate sensor. For
 272 example, the offset between sensors i and j in different sets, related through sensors k
 273 and l in the second round, would be $\Delta T_{ij} = \Delta T_{ik} + \Delta T_{kl} + \Delta T_{lj}$. For sensors related
 274 through the third round an additional term should be added, further increasing the offset
 275 uncertainty.

276 Offset repeatability is a critical parameter to understand, as the laboratory calibration
 277 must remain valid when applied to the actual detector. To study this, four independent
 278 calibration runs were performed for each set of four sensors. However, due to concerns
 279 about thermal fatigue in the primary reference sensor—subjected to 64 thermal cycles
 280 over the four repeatability runs—three secondary reference sensors were employed to
 281 regularly monitor its response and ensure reliability over time.

282 The following procedure is applied for each set of four sensors. First, they are placed
 283 inside the aluminium capsule. The central connector closer to the red one is used for
 284 the reference sensor. These positions are easily called by numbers from 1 (orange) to 4
 285 (red), as shown in Fig. 8-left.

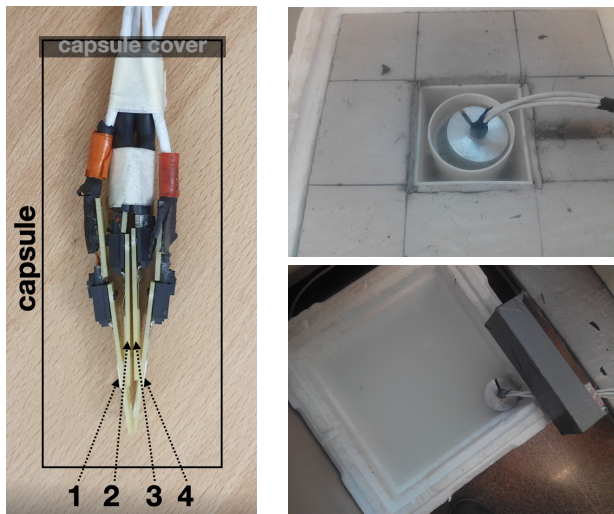


Figure 8: Left: Picture of sensor order inside the flask. Position 1 corresponds to highest serial number and 4 to lowest; position 3 is reserved to reference sensor. Top: Flask partially introduced in LAr. Bottom: Flask partially introduced in room water to warm up sensors before performing a new measurement.

286 After filling the PLA box with liquid argon, the aluminum capsule is partially im-
 13

mersed (see Fig. 8-right-top), allowing the air inside to cool down gradually. This setup prevents the sensors from coming into direct contact with liquid argon, instead inducing a slow cooldown through the surrounding cold gas atmosphere, thereby avoiding thermal shock. When the monitored temperature approaches the one of LAr (< 95 K), which takes about 15 minutes, the capsule is completely immersed, being filled with liquid. The PLA box is then completely filled with LAr to account for evaporation during the cool-down phase. Finally, the polystyrene vessel is closed using the polystyrene lid. The calibration run actually begins at that point and lasts for 40 minutes.

When the measurement is finished, the capsule is extracted from the liquid, emptied of LAr and partially immersed into another polystyrene box filled with water at room temperature (see Fig. 8-right-bottom). The warm-up process takes about ten minutes. When sensors have reached a temperature around 250 K a new independent calibration run can start.

Fig. 9 shows the typical evolution of the temperature for the four sensors in the capsule during the warm-up and cool-down processes. A sudden fall to 87 K is observed at minute 32, which corresponds to total immersion of the sensors in LAr. Notice also that two of the sensors have lower temperature during the cool-down process; those are sensors 1 and 4, the ones closer to the capsule walls.

For each set of sensors the procedure described above is repeated four times, resulting in four independent measurements of the same offset. These measurements are used to compute a mean offset value and its standard deviation (repeatability from now on).

4.3. Calibration results

Here we present the results of the calibration using both calibration methods, a study of the consistency of these results, and a preliminary estimation of the systematic uncertainty of the calibration process.

4.3.1. Results on the first round of measurements

Fig. 10 shows the offset of three different sensors with respect to the reference sensor as a function of time, and for four independent calibration runs. The offset is more stable for the sensor closer to the reference (position 2), while external sensors (positions 1 and 4) present larger variations, but show similar patterns between them. This effect is attributed to the geometry of the system, with sensors at different heights and not

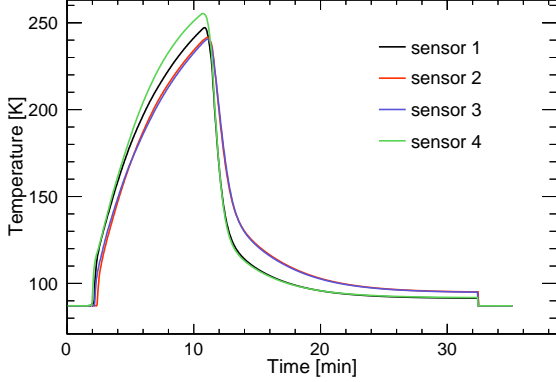


Figure 9: Temperature evolution between two calibration runs, showing the warm-up and cool-down phases of the four temperature sensors inside the capsule. Sensors 1 and 4 are located closest to the capsule walls.

³¹⁸ symmetrically positioned with respect to the capsule walls. This was taken into account
³¹⁹ when developing the second version of the system, presented in Sec. 5.

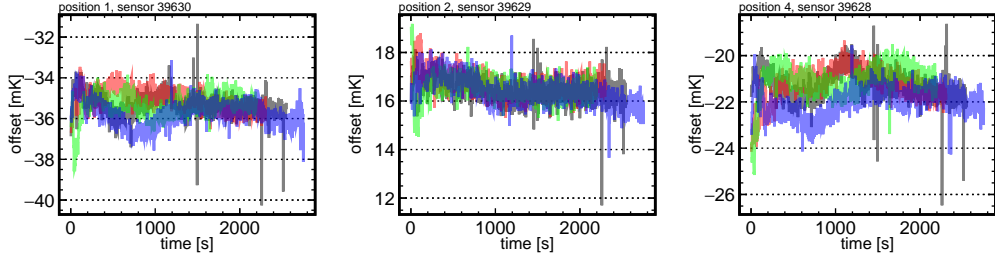


Figure 10: Offset between the reference sensor and each of the three sensors in a set, as a function of time. Each colour represents an independent calibration run.

³²⁰ The mean offset for each sensor and each calibration run is calculated as the average
³²¹ over the time interval between 1000 and 2000 seconds, identified as the most stable region
³²² for the majority of the runs. The standard deviation of the four means is taken as the
³²³ uncertainty, hereafter referred to as repeatability. As shown in Fig. 11, the uncertainties
³²⁴ are generally below 1 mK, demonstrating the high level of repeatability achieved in the
³²⁵ calibration process.

³²⁶ 4.3.2. Time walk correction for reference sensors

³²⁷ Time evolution of the response of sensor 39606 was studied by periodically (every \sim 20
³²⁸ immersions) computing its offset with respect to three secondary reference sensors, 39603,

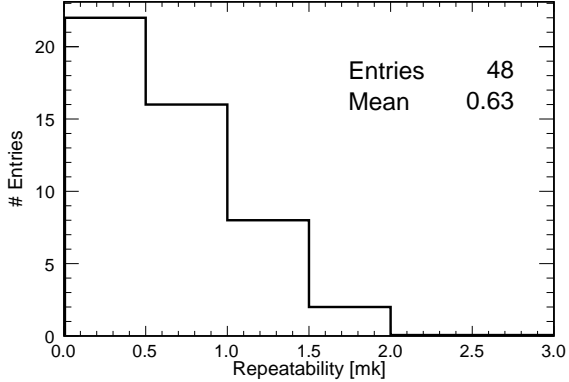


Figure 11: Distribution of the repeatability for calibration runs in the first round.

329 39604 and 39605. For each of those additional calibrations, two runs were taken instead
 330 of four in order to minimize thermal fatigue of the reference sensor. As shown in Fig. 12-
 331 left, the offset, computed as the mean of those two runs, varies linearly at a rate of
 332 0.07 mK/immersion, which suddenly increases to 0.22 mK/immersion after 60 runs.
 333 This change in the slope may be related with to the frequency of immersions, which
 334 increased from 3/day to 5/day. Sensor 39606 was initially used for other purposes, and
 335 the calibration of the 48 sensors conforming the static TGM started approximately at
 336 immersion 40. Given this change in its response, sensor 39606 was substituted by 39656
 337 as primary reference for the last quarter of the TGM calibration in order to avoid further
 338 fatigue and potential untraceable behaviour. The evolution of the new reference sensor
 339 is shown in Fig. 12-right. It is worth noting that the same slopes are valid for the three
 340 secondary reference sensors in both cases, supporting the idea that the change observed
 341 in the offsets can be exclusively attributed to thermal fatigue of the reference sensor.

342 The zero intercept in both panels of Fig. 12 corresponds to the unbiased offset (or the
 343 offset at $N_{\text{immersions}} = 0$) of each of the secondary reference sensors with respect to the
 344 primary reference. In order to compute the unbiased offset for a sensor s , a time walk
 345 correction after N immersions is parameterised as:

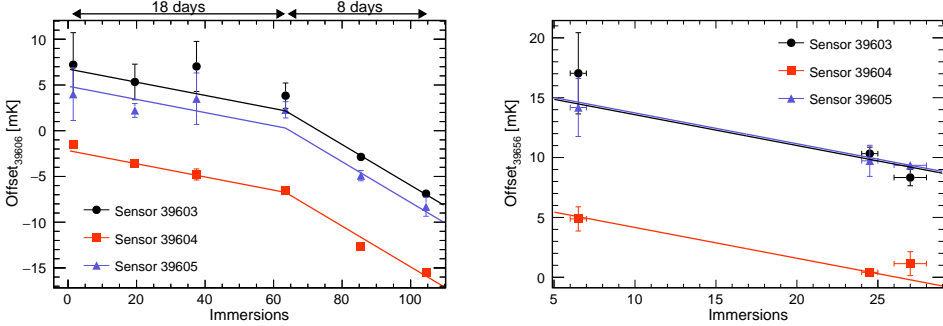


Figure 12: Offset between the reference sensors (39606 on the left panel and 39656 on the right panel) and the three secondary references as a function of the number of immersions. Offsets for sensor 39604 have smaller errors because of its position inside the capsule. Solid lines correspond to the parametrization in Eq. 4.

$$\Delta T_{s,06}(N = 0) = \begin{cases} \Delta T_{s,06}(N) + (0.072 \pm 0.003) * N & N < 63.5 \\ \Delta T_{s,06}(N) + (0.072 \pm 0.003) * 63.5 + \\ \quad +(0.223 \pm 0.007) * (N - 63.5) & N > 63.5, \end{cases} \quad (4)$$

$$\Delta T_{s,56}(N = 0) = \Delta T_{s,56}(N) + (0.168 \pm 0.007) * N. \quad (5)$$

346 All sensors can be related to the same primary reference sensor, 39606, adding the
 347 unbiased offset between sensors 39606 and 39656, $\Delta T_{56,06}(N = 0)$, to sensors calibrated
 348 with respect to 39656. By averaging over the three secondary reference sensors, the value
 349 obtained is $\Delta T_{56,06}(N = 0) = -9.19 \pm 0.13$ mK.

350 *4.3.3. Results on the reference method*

351 Fig. 13 shows the offset of all sensors with respect to the 39606 reference. As it can
 352 be noticed, the dispersion of the offsets is compatible with 0.1 K, the value quoted by
 353 the vendor. Fig. 14-left shows the distribution of the repeatability of the computed
 354 calibration constants after applying the different corrections, showing an average value
 355 below 1 mK.

356 *4.3.4. Results on the tree method*

357 The offsets are computed in this case with respect to an arbitrary reference among all
 358 sensors being calibrated. Selecting as reference a sensor present in the third round (see

359 Fig. 7) minimizes the number of operations required to compute the offsets, thereby
 360 reducing the associated uncertainty. Sensor 39645 was chosen as reference. Fig. 14-right
 361 shows the distribution of the repeatability of the computed calibration constants, the
 362 mean of which is slightly below the one obtained for the reference method. Thus, it
 363 is confirmed that despite the higher number of intermediate sensors to relate any two
 364 sensors, the additional uncertainty introduced by the time walk correction makes the tree
 365 method superior to the reference method. Moreover, the reference method introduces a
 366 —not yet known— systematic error associated to the time wall correction model.

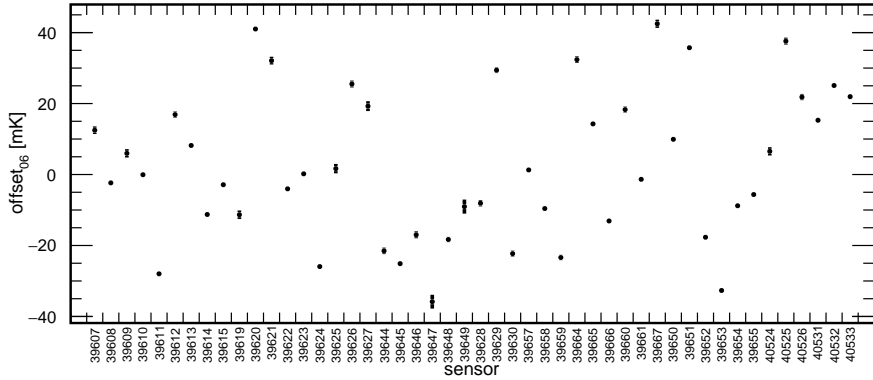


Figure 13: Offset of each sensor with respect to reference sensor 39606 using the reference method.

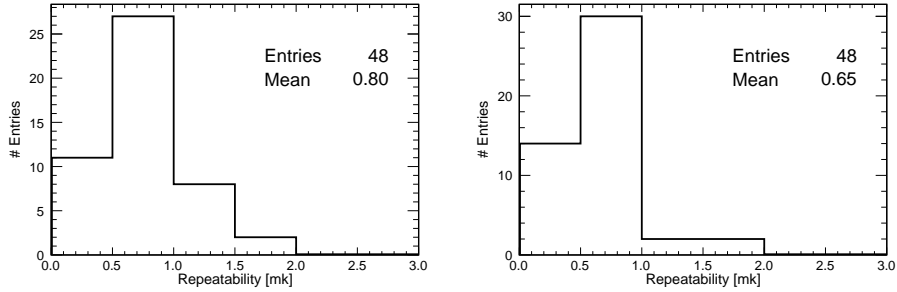


Figure 14: Left: repeatability distribution for the reference method. Right: repeatability distribution for tree method.

367 4.3.5. Consistency cross-check and error estimation

368 The uncertainties presented are, on average, smaller than 1 mK and correspond to the
 369 standard deviation of the four independent measurements of each calibration constant,

370 combined with the error propagation from the required corrections: time-walk correction
371 for the reference method, addition of calibration constants for the tree method, and the
372 uncorrected electronic residual offset common to both calibration methods. These correc-
373 tions likely include unknown systematic effects impacting the final calibration constants,
374 which need to be added to the systematic uncertainty associated to the assumption of
375 homogeneous temperature inside the capsule. To estimate the overall precision of the
376 calibration, the following cross-check was performed. The calibration strategy yields two
377 independent values for each sensor’s calibration constant—one obtained from the refer-
378 ence method and the other from the tree method. For the sixteen sensors used in the
379 second round of the calibration tree, these two values are linearly independent because
380 they are derived from different sets: the reference method relies solely on first-round
381 runs, while the tree method uses only second and third-round runs for those sensors.
382 Therefore, these sixteen sensors provide an effective basis for estimating the calibration
383 procedure’s precision by comparing the results obtained from the two methods.

384 By construction, the result of subtracting the calibration constants obtained in the
385 two methods should be compatible with the offset between sensors 39645 and 39606,
386 $\Delta T_{45,06} = \Delta T_{s,06} - \Delta T_{s,45} = T_{45} - T_{06}$, used as reference for the tree and reference
387 methods respectively. This offset is found to be -25.1 ± 0.7 mK by direct measurement of
388 the two sensors (see 10th column in Fig. 7 and 13). Fig. 15 shows this benchmark without
389 (left) and with (right) time walk corrections for the 16 sensors aforementioned, probing
390 the self-consistency of this correction. The standard deviation of this distribution, 2.4
391 mK (the width of the red band in Fig. 15-right), is an estimation of the quadratic sum
392 of the total uncertainty of both calibrations. Assuming that the reference sensor method
393 has a larger uncertainty than the tree method due to the time walk correction, an upper
394 limit of 1.7 mK for the total error of the tree method can be assumed. In the same way,
395 this is the inferior limit for the total error of the reference method. In both cases, these
396 errors are less than half of what was originally required for the temperature monitoring
397 system in DUNE FD-HD.

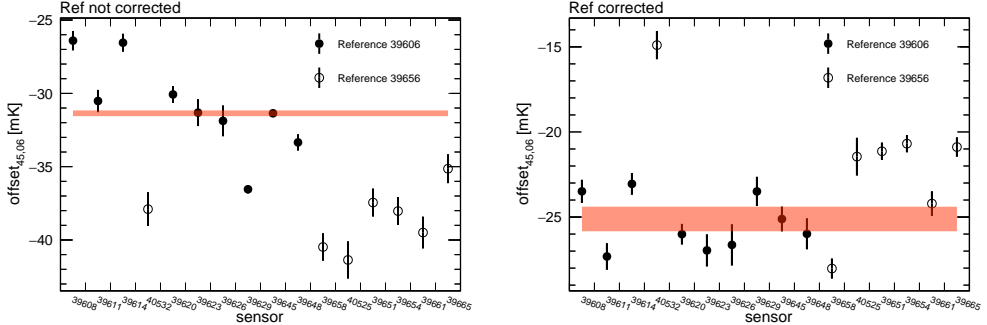


Figure 15: $\Delta T_{45,06}$ computed through all sensors of the second round of the calibration procedure. Left: not applying corrections. Right: applying corrections. A clear improvement is obtained using the corrections on the reference sensor. The red line represents the expected value of this calibration constant.

398 5. Re-calibration after ProtoDUNE-SP operation

399 After the decommissioning of ProtoDUNE-SP in 2020, the temperature sensors were
400 disconnected from the TGM and re-calibrated multiple times (see Table 1), using both
401 LAr and LN₂ as cryogenic media. Two sensors were damaged during the decommissioning
402 process and were not replaced until the LAr-2023 calibration campaign. The comparative
403 analysis of those re-calibrations not only offers insights into the long-term stability of the
404 sensors but also elucidates any potential dependencies on the choice of the cryogenic
405 liquid. Although DUNE will use LAr, massive RTD calibration would benefit from using
406 LN₂, given its higher accessibility and lower cost.

Date	Cryogenic liquid	# Sensors in capsule
March 2018	LAr	4
February 2022	LN ₂	14
March 2023	LN ₂	14
July 2023	LAr	14

Table 1: Calibration runs with indication of the date, the cryogenic liquid used and the number of sensors inside the capsule.

407 In this section, a description of the setup used for these new calibrations, the changes
408 applied to the procedure as well as the results and conclusions of these calibrations are
409 presented.

410 *5.1. Evolution of the calibration setup*

411 The FD-HD module will be equipped with over 500 precision sensors [9], making the use
412 of the current calibration setup impractical, as it can accommodate only four sensors
413 simultaneously. Significant modifications have been introduced in order to increase this
414 number to twelve, while maintaining the precision achieved during the 2018 calibration
415 campaign. This was accomplished by positioning sensors at the same height, to avoid
416 any potential vertical gradient, and following a cylindrical configuration, under the as-
417 sumption that convection inside the capsule has rotational symmetry. This symmetry
418 is also kept outside the capsule in all concentric cryogenic containers, having added a
419 fourth independent volume which should further reduce convection inside the inner cap-
420 sule. This notable advancement greatly streamlines the calibration process and serves
421 to reduce both statistical and systematic errors associated with the procedure. Fig. 16
422 shows the different elements of the new calibration setup, which are described below:

- 423 • A polystyrene box with dimensions $55 \times 35 \times 30 \text{ cm}^3$ and 4.5 cm thick walls with
424 a dedicated cover of the same material.
- 425 • Extruded polystyrene rectangles with a cylindrical hole of 12.5 cm diameter and
426 25 cm height, to conform the inner volume.
- 427 • A PTFE container with 12.5 cm diameter, 25 cm height and 2 mm thick walls to
428 fit in the hole left in the box. The approximate volume is 2 L.
- 429 • A 3D printed PLA cylinder with two independent concentric volumes, placed inside
430 the PTFE container.
- 431 • A cylindrical aluminum capsule to be placed in the inner volume of the PLA cylin-
432 der. It has 7 cm diameter, 14 cm height and 1 mm thick walls.
- 433 • A 3D printed PLA holder for 14 sensors, 12 of them forming a circle (the ‘corona’)
434 and the other 2 at the center, to be used as references. This support can be attached
435 to the aluminum capsule at a fixed height. Cables are naturally extracted from the
436 top of the assembly. A detailed view of this holder can be found in Fig. 16.
- 437 • The readout electronics, described in Sec. 3 has been retained from the previous
438 setup.

- 439 • A more cost effective cable with similar performance has been used. Produced by
 440 TempSens [27], it has four twisted cables instead of two separated twisted pairs
 441 and an additional Kapton insulation layer between the shielding mesh and the four
 442 conductors. Its diameter is 2.7 mm.

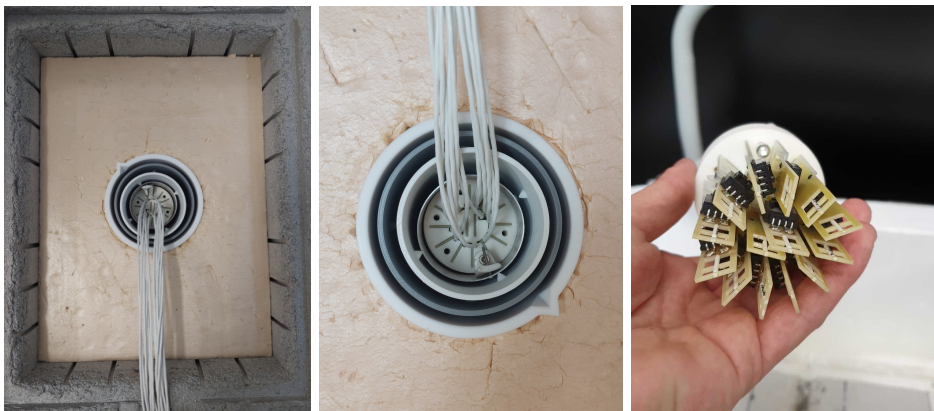


Figure 16: Left: The polystyrene box that hosts the calibration setup. Middle: Detail of the four concentric independent volumes conforming the calibration setup. Right: The 12 corona sensors plus the 2 references.

443 *5.2. Calibration procedure*

444 The sensor support was originally designed to accommodate two reference sensors in
 445 the center (see Fig. 16), enabling both the reference and tree calibration methods.
 446 However, it was soon observed that temperature variations between corona and reference
 447 sensors were significantly larger than those between any two corona sensors. This effect
 448 is attributed to the convection pattern inside the capsule, which is expected to have
 449 rotational invariance, and hence favour sensors disposed following a cylindrical symmetry.
 450 This can be observed in Fig. 17-left, where the offset between two corona sensors is
 451 nearly constant in time in four independent measurements, and in Fig. 17-right, where
 452 the offset between a corona and a reference sensor shows a more chaotic behaviour.
 453 Consequently, only the ‘tree’ calibration method was considered during the calibrations
 454 after ProtoDUNE-SP decommissioning.

455 The new calibration tree, shown in Fig. 18, contemplates four 12-sensors sets in the
 456 first round, and a unique second round with three promoted sensors from each of the

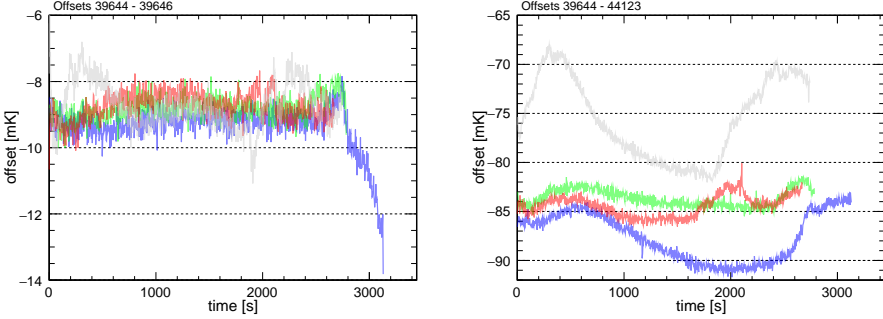


Figure 17: Left: The 4 measured offsets between two arbitrary sensors in the corona. Right: The 4 measured offsets between a sensor in the corona and one of the references, at the center.

457 sets in the first round. With this scheme, promoted sensors only suffer 8 baths, avoiding
 458 the necessity of a time-walk correction.

459 The experimental procedure is similar to the one presented in Sec. 4. Two small
 460 variations were introduced. First, the several concentric containers are cooled down
 461 for 40 minutes before introducing the aluminium capsule for the first time in a day,
 462 slightly improving the results of the first calibration run. Second, the warm up process
 463 is accelerated using a heat gun, avoiding the use of water.

464 5.3. Calibration results

465 A sensor from the second round is chosen as the reference, as this minimizes the number of
 466 operations required for the non-promoted sensors. Since each set includes three promoted
 467 sensors, there are three linearly independent ways to compute the offset relative to the
 468 reference for the nine non-promoted sensors in that set. The calibration constant for these
 469 sensors is calculated as the weighted average of the three “paths”, with its uncertainty
 470 given by the standard deviation of these three values. The offset uncertainty used in the
 471 weighted average for each of the three paths is computed by quadratically summing the
 472 individual uncertainties (as in Fig. 19) of all terms contributing to the offset along that
 473 specific path. Sensor 40525 is adopted as the reference for the remainder of the analysis.

474 Fig. 19 shows the distribution of the repeatability (defined in Sec. 4.3.1) for the three
 475 new calibrations mentioned in Table 1. The values obtained are slightly worst than in
 476 the 2018 calibration campaign, which is somehow expected given the increased capsule
 477 size and the larger distance between sensors. This hypothesis is supported by Fig. 20,

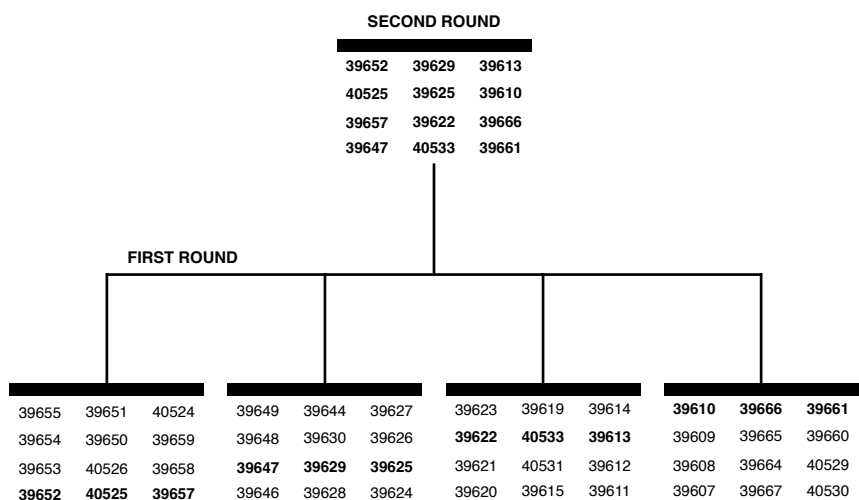


Figure 18: Schematic of the calibration sequence used with the new setup. Each of the sets contains 12 sensors, all of them placed in the corona, plus 2 references at the center. Sensors in bold in the first round are promoted to the second round.

478 showing the repeatability as a function of the distance to the reference sensor in the
 479 corona for a particular measurement. However, there is no substantial difference between
 480 the repeatability obtained for LN2 and LAr calibrations.

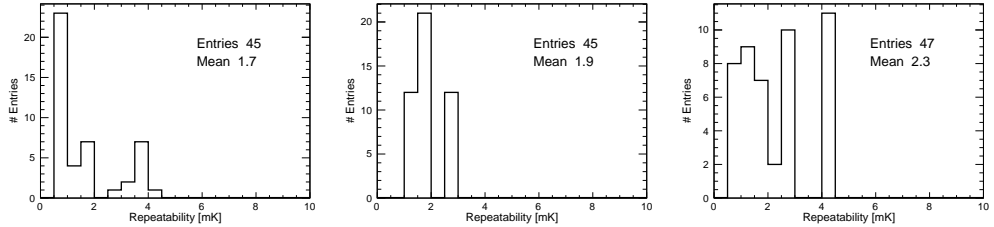


Figure 19: Repeatability distribution for the new calibrations. Left: LN2-2022. Middle: LN2-2023. Right:LAr-2023. LAr-2023 includes two additional sensors, absent from earlier calibration campaigns, which were replaced after being damaged during the decommissioning of ProtoDUNE-SP.

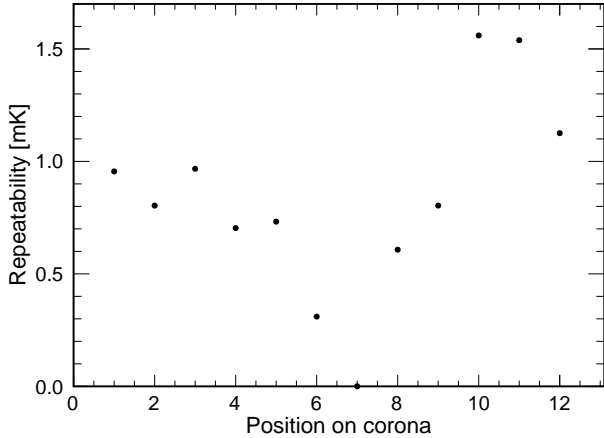


Figure 20: Repeatability as a function of position in the corona for the first set of the LAr-2023 calibration campaign. Sensor in position 7 is taken as reference.

481 Comparison between LN2 and LAr calibrations can also be used to understand the
 482 dependence of the calibration constants on the absolute temperature. This is shown
 483 in Fig. 21 along with other comparisons between calibration campaigns. The standard
 484 deviation of the distribution is lower when comparing two calibrations in the same liquid
 485 (LN2 in this case). However no bias is observed when comparing calibrations in two
 486 different liquids, indicating that offsets are insensitive to a 10 K variation in absolute
 487 temperature.

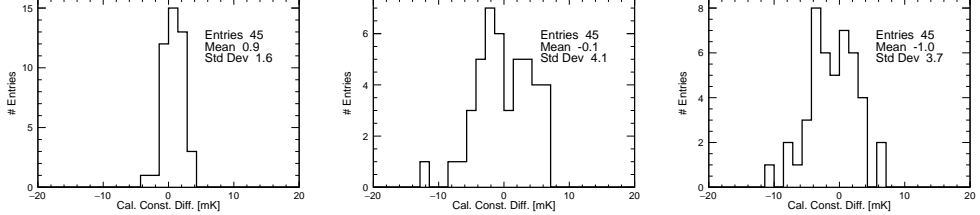


Figure 21: Difference between offsets for two calibrations. Left: LN2-2022 and LN2-2023. Middle: LN2-2022 and LAr-2023. Right: LN2-2023 and LAr-2023.

488 Ageing and long term stability have also been addressed. The left panel of Fig. 21
 489 shows no difference between the offsets calculated in LN2 with a delay of one year. A bet-
 490 ter understanding of this effect is achieved by comparing with the LAr-2018 calibration,
 491 as shown in the next section.

492 5.4. Comparison between new and old calibrations

493 Fig. 22 shows the distribution of the offset difference between the LAr-2018 and LAr-
 494 2023 calibrations. The mean of the distribution is -0.1 ± 0.6 mK, excluding any relevant
 495 systematic drift. The standard deviation of the distribution, 4.3 mK, is only slightly
 496 larger than the ones obtained in the comparison between newer calibrations, which could
 497 be due to the unknown contribution of the uncorrected readout offsets, pointing to small
 498 or non-existing ageing effects. This can also be observed in Table 2, summarizing the
 499 results of all possible comparisons between calibration campaigns, showing the mean and
 500 standard deviation of those comparisons. The lowest standard deviation, 1.6 mK, is
 501 obtained for the LN2-2022 to LN2-2023 combination, which is somehow expected since
 502 i) the cryogenic liquid is the same, ii) ageing should be small since there is only one year
 503 difference and iii) having use the same readout channels, readout offsets cancel out.

	LAr-2018	LN2-2022	LN2-2023	LAr-2023
LAr-2018	-	0.0, 3.5	0.9, 3.9	-0.1, 4.3
LN2-2022	-	-	0.9, 1.6	-0.1, 4.1
LN2-2023	-	-	-	-1.0, 3.7
LAr-2023	-	-	-	-

Table 2: Mean and standard deviation of the difference between the calibration constants obtained in two calibration campaigns.

504 The difference between the constants obtained in two calibration campaigns can be used

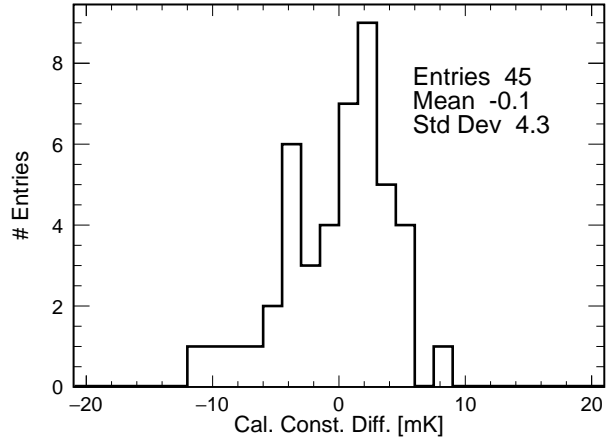


Figure 22: Difference between offsets for LAr-2018 and LAr-2023 calibration campaigns.

505 to estimate the total calibration error. Since ProtoDUNE Horizontal Drift (ProtoDUNE-
 506 HD), the next iteration of the ProtoDUNE-SP detector, and DUNE will use LAr, the
 507 best estimation of the error would come from a LAr to LAr comparison close in time to
 508 the actual detector running. Being this combination not available, three other combina-
 509 tions can be used. The comparison between the LN2 calibrations from 2022 and 2023
 510 yields a standard deviation of 1.6 mK, which should represent the quadratic sum of the
 511 individual calibration errors. Assuming equal errors for both campaigns, this implies a
 512 single calibration error of approximately 1.13 mK. In this case, readout channel offsets
 513 cancel out, although real fluctuations in those offsets still contribute to the estimated
 514 single calibration error. The comparison between LAr calibrations from 2018 and 2023
 515 provides further insight, with a standard deviation of 4.3 mK, corresponding to a sin-
 516 gle calibration error of about 3.0 mK. However, this value includes uncorrected readout
 517 offsets as well as potential effects from sensor ageing. Finally, comparing the new LAr
 518 and LN2 calibration campaigns avoids issues related to readout offsets and ageing but
 519 may be affected by the differences in cryogenic liquids. These comparisons yield a similar
 520 standard deviation around 3.8 mK, implying a single calibration error of approximately
 521 2.7 mK. This value thus establishes an upper limit on the LAr calibration error. In
 522 summary, the individual calibration error in LAr is estimated to lie between 1.6 and
 523 3.0 mK. This range is consistent with an independent estimate of 1.7 mK obtained using

524 a different method for the LAr-2018 calibration (see Sec. 4.3.5).

525 **6. Conclusions**

526 The DUNE experiment will require the construction and operation of the largest cryostats
527 ever used in a particle physics experiment. This makes the continuous measurement of
528 temperature gradients in liquid argon crucial for monitoring the stability of the cryogenics
529 system and for detector calibration. R&D on the calibration of RTD probes started in
530 2017, leading to promising results for sensors installed in the DUNE prototype at CERN.

531 The first setup proved the viability of the method, obtaining a calibration error of 1.7
532 mK. A key component was the readout electronics, with an intrinsic resolution better
533 than 0.5 mK in the comparison between two channels. The mechanics was also crucial,
534 with several insulation layers consisting of independent concentric volumes, ensuring
535 minimal convection in the inner volume. Sensors were contained in an aluminium capsule,
536 enabling slow cool-down and warm-up processes, found to be fundamental to guarantee
537 the integrity of the sensors and to minimize the effect of ageing.

538 The calibration system was later enhanced to accommodate the large-scale calibration
539 required for the DUNE detectors. The capacity of the inner capsule was increased from
540 4 to 14 sensors, while improvements were made to the insulation and symmetry of the
541 system to minimize temperature differences between sensors. The new system has slightly
542 worst repeatability for sensors in the same set, but reduces the statistical and systematic
543 errors associated to the calibration tree, needed to relate any two sensors in different
544 calibration sets. Calibration with the new setup has achieved a precision in the range of
545 1.6-3.0 mK, substantially better than the 5 mK DUNE requirement.

546 Another difference between the new and old calibrations is the use of a different
547 cryogenic liquid. While DUNE will use LAr, LN₂ is cheaper, simplifying the process of
548 massive calibration for DUNE detectors. The 10 K difference between those liquids has
549 a minimal effect on the calibration constants.

550 A comparison of the four calibration campaigns has provided valuable insights into
551 aging effects, with no evidence of RTD aging observed over a five-year period. This
552 highlights the stability and reliability of the PT-102-based system.

553 **7. Acknowledgments**

554 The present research has been supported and partially funded by Conselleria d'Innovació,
555 Universitats, Ciència i Societat Digital, by the Fundación 'La Caixa', and by MICINN.
556 The authors would also like to thank all the people involved in the installation,
557 commissioning and operation of ProtoDUNE-SP, specially to Stephen Ponders.

558 **References**

- 559 [1] B. Abi, et al., Deep Underground Neutrino Experiment (DUNE), Far Detector Technical Design
560 Report, Volume I Introduction to DUNE, JINST 15 (08) (2020) T08008. [arXiv:2002.02967](https://arxiv.org/abs/2002.02967), doi:
561 [10.1088/1748-0221/15/08/T08008](https://doi.org/10.1088/1748-0221/15/08/T08008).
- 562 [2] B. Abi, et al., Long-baseline neutrino oscillation physics potential of the DUNE experiment, Eur.
563 Phys. J. C 80 (10) (2020) 978. [arXiv:2006.16043](https://arxiv.org/abs/2006.16043), doi:[10.1140/epjc/s10052-020-08456-z](https://doi.org/10.1140/epjc/s10052-020-08456-z).
- 564 [3] B. Abi, et al., Deep Underground Neutrino Experiment (DUNE), Far Detector Technical Design
565 Report, Volume II: DUNE Physics (2 2020). [arXiv:2002.03005](https://arxiv.org/abs/2002.03005).
- 566 [4] B. Abi, et al., Supernova neutrino burst detection with the Deep Underground Neutrino Experiment,
567 Eur. Phys. J. C 81 (5) (2021) 423. [arXiv:2008.06647](https://arxiv.org/abs/2008.06647), doi:[10.1140/epjc/s10052-021-09166-w](https://doi.org/10.1140/epjc/s10052-021-09166-w).
- 568 [5] B. Abi, et al., Prospects for beyond the Standard Model physics searches at the Deep Underground
569 Neutrino Experiment, Eur. Phys. J. C 81 (4) (2021) 322. [arXiv:2008.12769](https://arxiv.org/abs/2008.12769), doi:[10.1140/epjc/s10052-021-09007-w](https://doi.org/10.1140/epjc/s10052-021-09007-w).
- 570 [6] S. Amerio, et al., Design, construction and tests of the ICARUS T600 detector, Nucl. Instrum.
571 Meth. A 527 (2004) 329–410. doi:[10.1016/j.nima.2004.02.044](https://doi.org/10.1016/j.nima.2004.02.044).
- 572 [7] R. Acciarri, et al., Design and Construction of the MicroBooNE Detector, JINST 12 (02) (2017)
573 P02017. [arXiv:1612.05824](https://arxiv.org/abs/1612.05824), doi:[10.1088/1748-0221/12/02/P02017](https://doi.org/10.1088/1748-0221/12/02/P02017).
- 574 [8] B. Abi, et al., The Single-Phase ProtoDUNE Technical Design Report (6 2017). [arXiv:1706.07081](https://arxiv.org/abs/1706.07081).
- 575 [9] B. Abi, et al., Deep Underground Neutrino Experiment (DUNE), Far Detector Technical Design
576 Report, Volume IV: Far Detector Single-phase Technology, JINST 15 (08) (2020) T08010. [arXiv:2002.03010](https://arxiv.org/abs/2002.03010), doi:[10.1088/1748-0221/15/08/T08010](https://doi.org/10.1088/1748-0221/15/08/T08010).
- 577 [10] B. Abi, et al., First results on ProtoDUNE-SP liquid argon time projection chamber performance
578 from a beam test at the CERN Neutrino Platform, JINST 15 (12) (2020) P12004. [arXiv:2007.06722](https://arxiv.org/abs/2007.06722), doi:[10.1088/1748-0221/15/12/P12004](https://doi.org/10.1088/1748-0221/15/12/P12004).
- 579 [11] A. A. Abud, et al., Design, construction and operation of the ProtoDUNE-SP Liquid Argon TPC,
580 JINST 17 (01) (2022) P01005. [arXiv:2108.01902](https://arxiv.org/abs/2108.01902), doi:[10.1088/1748-0221/17/01/P01005](https://doi.org/10.1088/1748-0221/17/01/P01005).
- 581 [12] Y. Xiao, Purity monitoring for ProtoDUNE-SP, J. Phys. Conf. Ser. 2156 (2021) 012211. doi:
582 [10.1088/1742-6596/2156/1/012211](https://doi.org/10.1088/1742-6596/2156/1/012211).
- 583 [13] M. Adamowski, et al., The Liquid Argon Purity Demonstrator, JINST 9 (2014) P07005. [arXiv:1403.7236](https://arxiv.org/abs/1403.7236), doi:[10.1088/1748-0221/9/07/P07005](https://doi.org/10.1088/1748-0221/9/07/P07005).
- 584 [14] D. L. Adams, et al., Design and performance of a 35-ton liquid argon time projection chamber
585 as a prototype for future very large detectors, JINST 15 (03) (2020) P03035. [arXiv:1912.08739](https://arxiv.org/abs/1912.08739),
586 doi:[10.1088/1748-0221/15/03/P03035](https://doi.org/10.1088/1748-0221/15/03/P03035).
- 587 [15] A. Hahn, M. Adamowski, D. Montanari, B. Norris, J. Reichenbacher, R. Rucinski, J. Stewart,
588 T. Tope, The LBNE 35 Ton Prototype Cryostat, in: 2014 IEEE Nuclear Science Symposium and
589 Medical Imaging Conference and 21st Symposium on Room-Temperature Semiconductor X-ray and
590 Gamma-ray Detectors, 2016. doi:[10.1109/NSSMIC.2014.7431158](https://doi.org/10.1109/NSSMIC.2014.7431158).
- 591 [16] Minco, Resistance thermometry, last visited: 2023-05-18.
592 URL <https://www.minco.com/wp-content/uploads/Resistance-Thermometry.pdf>
- 593 [17] LakeShore, Platinum sensors applications, last visited: 2023-05-18.
594 URL <https://www.lakeshore.com/products/categories/overview/temperature-products/cryogenic-temperature-sensors/platinum>
- 595 [18] Molex, Idc-4 male connector, last visited: 2025-06-05.
596 URL <https://www.molex.com/en-us/products/part-detail/0014562042?display=pdf>
- 597 [19] Molex, Idc-4 female connector, last visited: 2025-06-05.
598 URL <https://www.molex.com/en-us/products/part-detail/0015943043?display=pdf>

- 604 [20] Axon, Axon custom cables, last visited: 2022-10-01.
605 URL https://www.axon-cable.com/en/00_home/00_start/00/index.aspx
- 606 [21] M. A. García-Peris, ProtoDUNE T-Gradient development and calibration, Master's thesis, Valencia
607 U. (7 2018). doi:10.2172/1780813.
- 608 [22] E. Chojnacki, A Multiplexed RTD Temperature Map System for Multi-Cell SRF Cavities, in:
609 SRF2009, Vol. TUPPO033, 2009, p. 232.
- 610 [23] B.-B. application bulletin, Implementation and applications of current sources and current receivers,
611 last visited: 2024-04-02.
612 URL <https://www.ti.com/lit/an/sboa046/sboa046.pdf?ts=1712062207089>
- 613 [24] Tektronix, Keithley 2001 digit high performance multimeter, last visited: 2024-04-02.
614 URL https://download.tek.com/datasheet/1KW-73954-1_2001-2002_DMM_Datasheet_080323.pdf
- 615 [25] N. Instruments, Compactrio systems, last visited: 2024-04-02.
616 URL <https://www.ni.com/es/shop/compactrio.html>
- 617 [26] N. Instruments, Ni-9238, last visited: 2024-04-02.
618 URL <https://www.ni.com/es-es/shop/model/ni-9238.html>
- 619 [27] TempSens, Rtd cables, last visited: 2024-03-15.
620 URL <https://tempsens.com/catalog/cables-wires/rtd-triad-cables.html>